SANDIA REPORT SAND81-2563 • Unlimited Release • UC-62e
Printed January 1982

Contact Stresses on a Thin Plate After Large Displacements to a Half Parabolic Surface

Rodney K. Wilson, Robert C. Reuter, Jr.

Prepared by
Sandia National Laboratories
Albuquerque, New Mexico 87185 and Livermore, California 94550
for the United States Department of Energy
under Contract DE-AC04-76DP00789

SF2900Q(8-81)

Issued by Sandia National Laboratories, operated for the United States Department of Energy by Sandia Corporation.

Printed in the United States of America
Available from
National Technical Information Service
U.S. Department of Commerce
5285 Port Royal Road
Springfield, VA 22161

NTIS price codes
Printed copy: $6.00
Microfiche copy: A01

SAND81-2563

CONTACT STRESSES ON A THIN PLATE AFTER LARGE DISPLACEMENTS TO A HALF PARABOLIC SURFACE*

Rodney K. Wilson
Robert C. Reuter, Jr.
Sandia National Laboratories
Albuquerque, NM 87185

Abstract

In a previous report a solution was obtained for the determination of all loads necessary to hold an initially flat, thin, elastic plate in the shape of a prescribed parabolic surface, following large displacement. These loads include spatially varying normal tractions distributed over the back surface of the plate, and a uniform shear force and bending moment applied along the opposing edges which become the rims of the parabola after deformation. In actual practice the edge loads are not present and, as a result, local displacement and stress variations arise creating what is known as an edge effect. Furthermore, if the full parabola is separated into two equal halves at the vertex another edge effect occurs. The analysis used to compute the local displacement and stress variations arising near the rim is repeated here to treat the absence of edge loads at the vertex. In addition to the normal stresses which arise, shear stresses result from the absence of the membrane reaction at the vertex, which was present in the case of the full parabolic surface. Correlation between the present theory and data from laser ray trace experiments is also presented.

*This work performed at Sandia National Laboratories supported by the U.S. Department of Energy under contract number DE-AC04-76DP00789.

TABLE OF CONTENTS

ILLUSTRATIONS

NOMENCLATURE

D	flexural rigidity of reflective surface
E_p	Young's modulus of reflective panel
f	focal length of parabola
h_a	thickness of adhesive
G_a	shear modulus of adhesive
h_p	thickness of reflective panel
k	stiffness of adhesive plus substructure
M_R	bending moment applied at rim to maintain true parabolic shape
M_V	bending moment applied at vertex to maintain true parabolic shape
N_V	membrane load at vertex to maintain true parabolic shape
P_C	contact pressure applied over back surface of reflective panel to maintain true parabolic shape
Q_R	shear force applied at rim to maintain true parabolic shape
$w_R(x)$	displacement of reflective surface at x due to edge effect at rim
$w_V(x)$	displacement of reflective surface at x due to edge effect at vertex
x,y	rectangular coordinates
β	panel-adhesive-substructure stiffness parameter
γ	panel-adhesive shear parameter
δ_2	second cross-over distance
ν	Poisson's ratio
$\sigma_R(x)$	normal contact stress at x due to edge effect at rim
$\sigma_V(x)$	normal contact stress at x due to edge effect at vertex
$\tau(x)$	shear contact stress at x due to edge effect at vertex

INTRODUCTION

A current line focusing solar collector design involves bonding two initially flat, thin, reflective surface panels to a parabolic substructure as shown in Fig. 1. In a previous report [1], a study was made to predict the magnitude, direction and distribution of contact stresses required to hold the reflective surface (made of a single thin glass panel), after experiencing large displacements, to a rigid parabolic substructure. Particular attention was focussed on the edge effect occuring near each rim; that is, the appearance of localized contact stresses of higher magnitude than those acting on the rest of the panel, and a corresponding deviation from the true parabolic shape. The edge effect resulted from the absence of mechanical loads at the rim which were otherwise required to maintain the nonzero curvature defined by the true parabolic shape. By forming the reflective surface with two panels, additional free edges are created at the vertex. Consequently, a second edge effect region appears, though its presence does not affect the results obtained for the rim. In this report, a study of the vertex edge effect is presented. The results again show a localized contact stress variation and a loss of the true parabolic shape at the vertex similar to that occurring at the rim, but of greater magnitude. In addition, the analysis predicts a localized shear distribution on the back surface of the reflective panel.

ANALYSIS

In Fig. 2, one of the reflective panels is shown with the loads necessary to maintain the parabolic shape defined by

$$y = \frac{x^2}{4f} \quad , \tag{1}$$

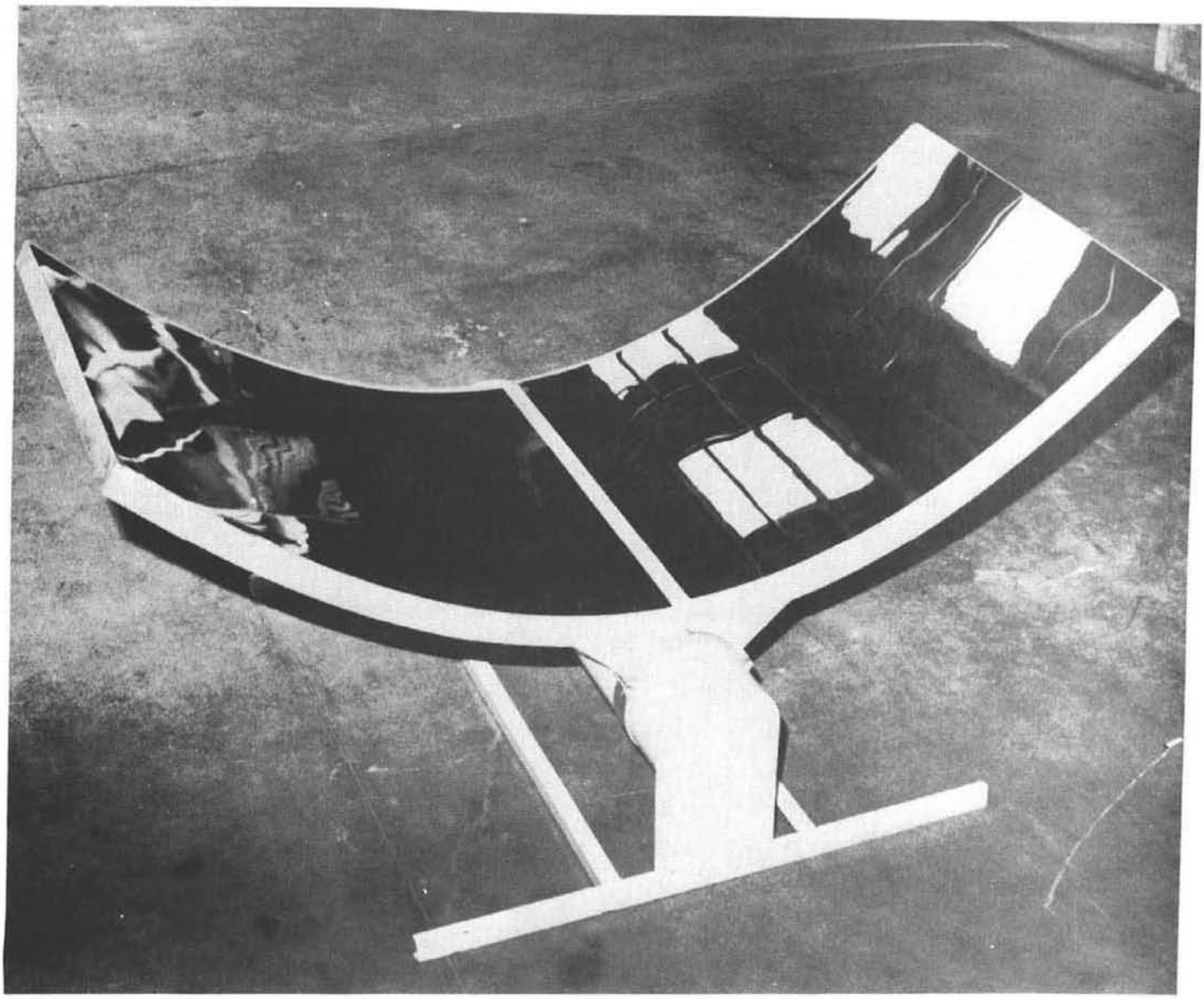

FIGURE 1. Assembled, parabolic, line focusing solar collector.

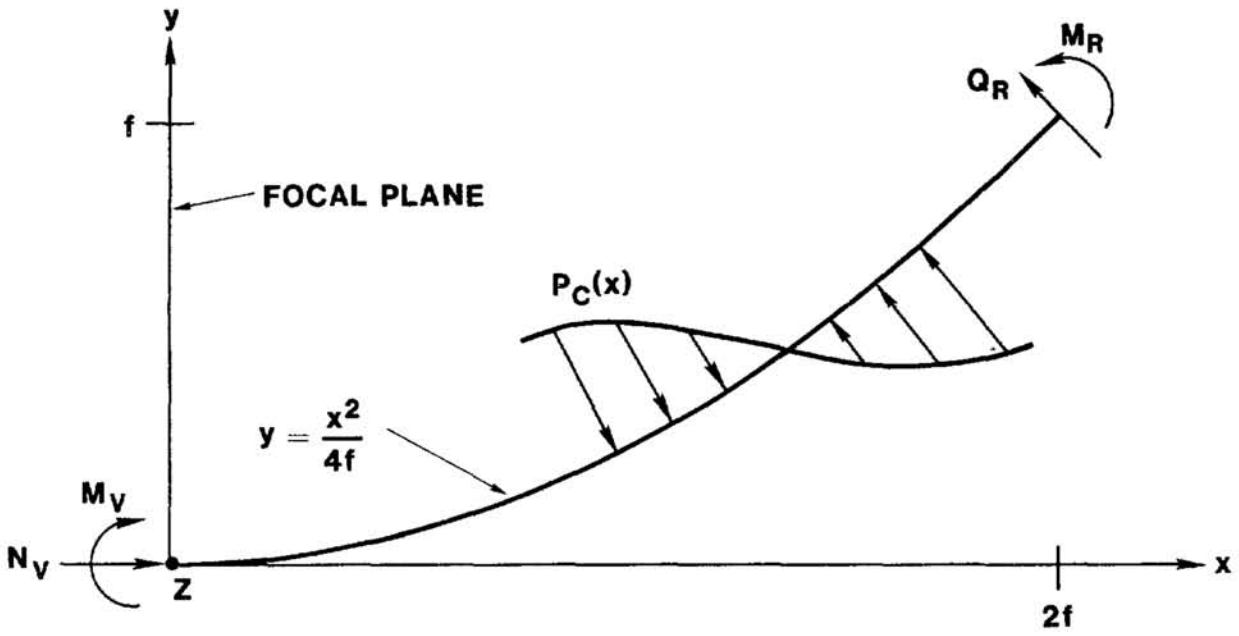

FIGURE 2. Diagram of half of the deformed, reflective surface explicating coordinates, rim and vertex loads and pressure distribution required to achieve the true parabolic shape.

where f is the focal length of the parabola. The loads shown in the figure have been calculated in [1] and are summarized below:

$$N_v = \frac{7D}{64f^2} \quad ,$$

$$M_v = \frac{D}{2f} \quad ,$$

$$Q_R = \frac{3D}{32f^2} \quad , \qquad (2)$$

$$M_R = \frac{\sqrt{2}\,D}{8f} \quad ,$$

$$P_C(x) = -\frac{5D}{16f^3\left[1+(x/2f)^2\right]^{3/2}} \left\{ -\frac{1}{40} + \frac{1}{1+(x/2f)^2}\left(6 - \frac{7}{1+(x/2f)^2}\right)\right\} .$$

D is the flexural rigidity of the reflective panel and is defined by

$$D = \frac{E_p h_p^3}{12(1-\nu^2)} \quad ,$$

where E_p is Young's modulus, ν is Poisson's ratio and h_p is the panel thickness. In [1] the residual loads at the rim, M_R and Q_R, were removed to satisfy the actual free edge conditions, and were replaced by equivalent normal tractions (contact stresses) applied to the back surface of the reflective panel and localized near the rim. This equivalent stress distribution, $\sigma_R(x)$, defined by

$$\sigma_R(x) = -\frac{\beta^3 D}{16(\beta f)^2} e^{-\beta(2f-x)} \left[\left(3+4\sqrt{2}(\beta f)\right)\cos\beta(2f-x) - 4\sqrt{2}\,(\beta f)\sin\beta(2f-x)\right], \qquad (3)$$

was shown to occur within a distance, δ_2, (referred to as the second cross-over distance) from the rim. It was possible to relate this distance to the material properties of the substructure through the relationship

$$\delta_2 = \frac{5\pi}{4\beta} \tag{4}$$

where

$$\beta = \sqrt[4]{\frac{k}{4D}} \quad . \tag{5}$$

Expression (4) is an approximation of

$$\beta - \beta\tan\beta(2f-x) + \frac{Q_R}{M_R} = 0 \ , \tag{6}$$

which defines the zeros of displacement or normal stress near the rim. To obtain (4), the quantity Q_R/M_R was neglected in comparison to β, based on the focal lengths of interest. In addition to introducing the stress distribution, removal of the rim loads resulted in a loss of the true parabolic shape. This loss was characterized by the rotation of the surface normals (slope error) defined by

$$w_R'(x) = \frac{1}{64(\beta f)^2}\, e^{-\beta(2f-x)} \left[\left(3+8\sqrt{2}(\beta f)\right)\cos\beta(2f-x) - 3\sin\beta(2f-x)\right]. \tag{7}$$

The expressions characterizing the stress distribution, σ_R, and the slope error, w_R', are shown graphically in Figs. 3 and 4 for various values of δ_2.

For the analysis of the two panel, or half parabola design the free edge at the vertex requires the removal of the vertex

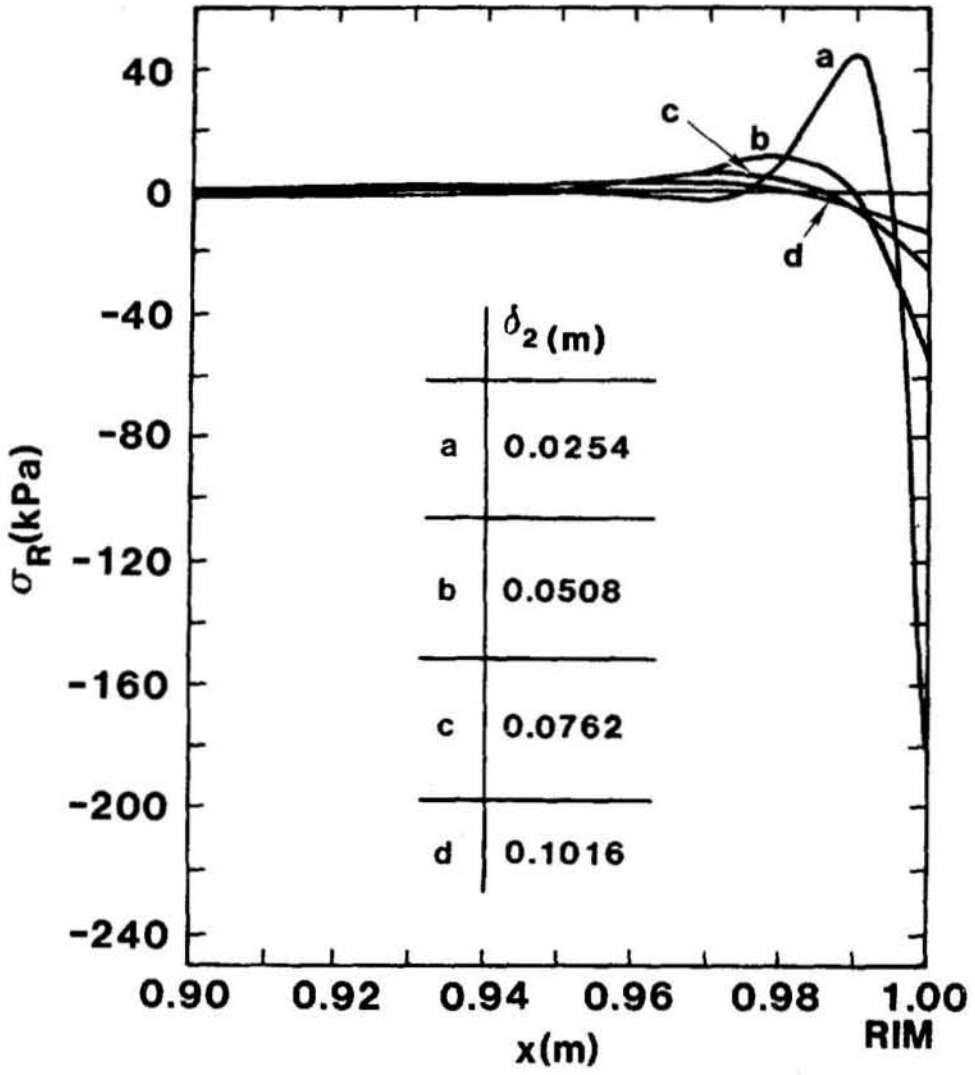

FIGURE 3. Contact stresses in adhesive applied to backside of deformed reflective surface arising from edge effect at rim.

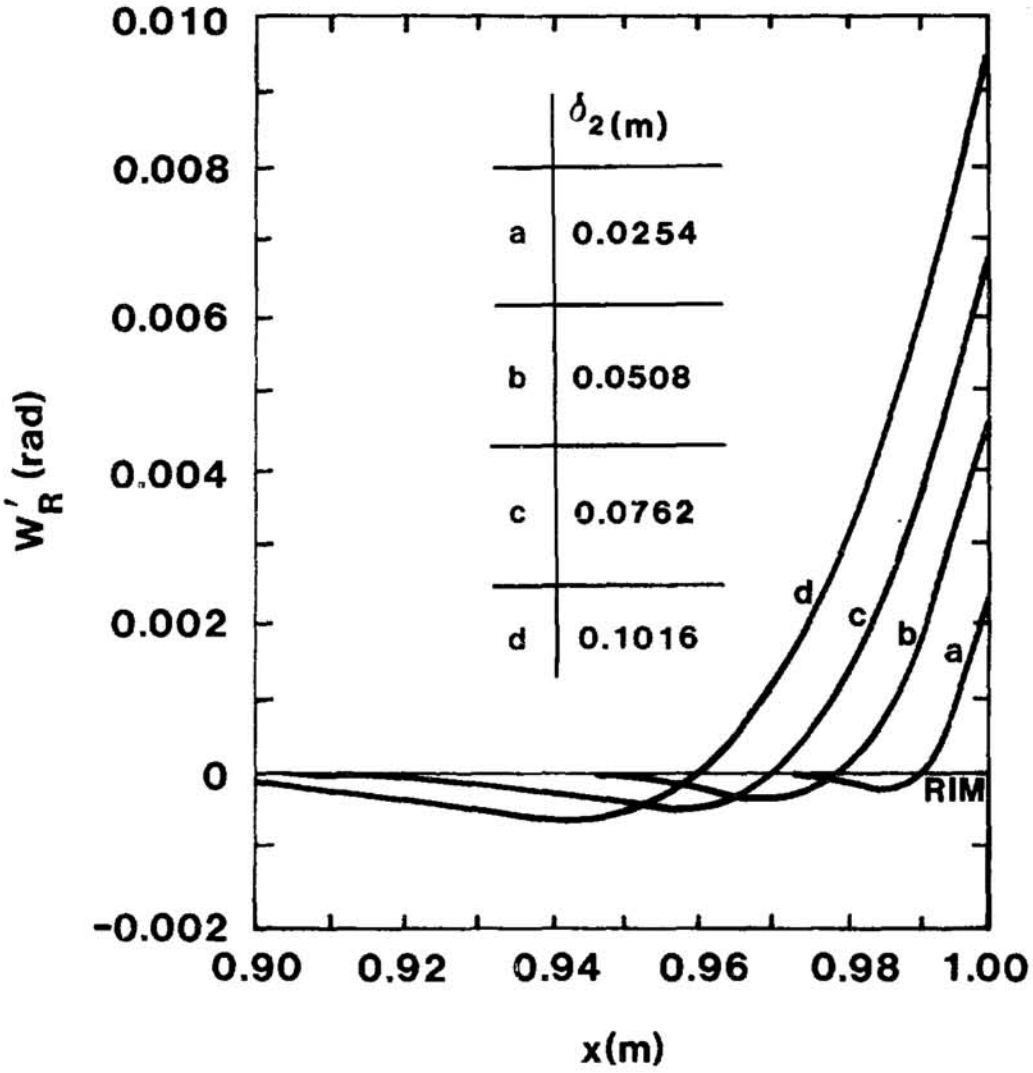

FIGURE 4. Rotation of surface normals (slope error) arising from edge effect at rim.

loads, N_V and M_V, to satisfy the actual boundary conditions. As in [1], they are replaced by equivalent stress distributions: the bending moment, M_V, is replaced by a normal stress distribution, $\sigma_V(x)$, and the axial force, N_V, is replaced by a shear stress distribution, $\tau_V(x)$. As with $\sigma_R(x)$, $\sigma_V(x)$ is obtained by considering a flat, semi-infinite plate on an elastic foundation with a bending moment equal in magnitude and opposite in direction to M_V applied to the end (Fig. 5). The arguments for modeling the edge region as a flat, semi-infinite plate are given in [1] and apply here as well. The resulting equation, the corresponding boundary conditions and the general solution corresponding to this problem are given by [2]

$$\frac{d^4 w_V}{dx^4} = - k w_V \quad , \tag{8}$$

$$D \left. \frac{d^3 w_V}{dx^3} \right|_{x=0} = 0 \quad , \tag{9}$$

$$D \left. \frac{d^2 w_V}{dx^2} \right|_{x=0} = 0 \quad , \tag{10}$$

$$w_V(x) = \frac{M_V}{2\beta^2 D} \, e^{-\beta x} \, [\sin\beta x - \cos\beta x] . \tag{11}$$

Computing the corresponding tension in the foundation gives the normal stress distribution in the adhesive, namely

$$\sigma_V(x) = k w_V(x) = 2 M_V \beta^2 e^{-\beta x} [\sin\beta x - \cos\beta x] . \tag{12}$$

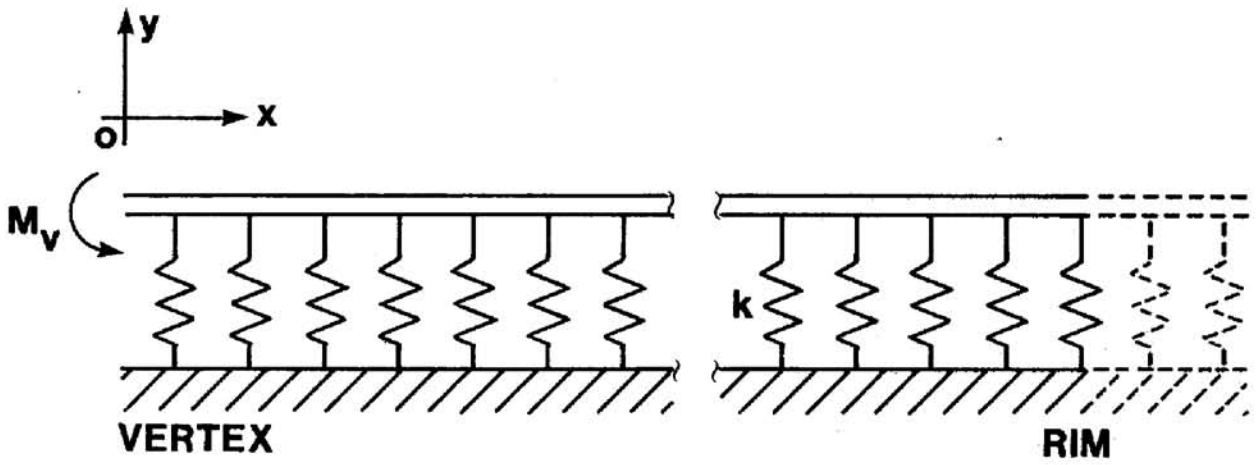

FIGURE 5. Diagram of the flat-plate model of the edge effect region at vertex explicating the coordinate system and semi-infinite extension.

Differentiating w with respect to x gives an expression for the slope error in the form

$$w_V'(x) = \frac{M_V}{\beta D} e^{-\beta x} \cos\beta x \quad . \tag{13}$$

General observations and optical measurements [4] of completed collectors suggest that the size of the edge effect zone at the vertex is approximately the same as it is at the rim. The present analysis verifies this through the definition of δ_2 which comes from the equation that defines the zeros of (11) or (12). The result is equation (6), but, with Q_R set equal to zero. This means that equation (4), which defines the size of the edge effect zone at the rim, also defines it at the vertex. The difference is that at the vertex, (4) is an exact definition of δ_2 whereas at the rim it is approximate. Calculations show, however, that for typical values of β, between 1.96 and 7.85 mm^{-1}, and a wide range of focal lengths, between 150.0 and 900.0 mm, the error resulting from the use of (4) at the rim is less than 3.0 percent (for the value of f = 480.8 mm used in the actual collector the error is less than 1.0 percent). On this basis, the present analysis predicts that the size of the edge effect zone, given by (4), is approximately the same at both the rim and the vertex, provided the values of the substructure stiffness (and hence the value of β) is also the same. Typical values of δ_2 are shown in Table 1 along with the corresponding stiffness, kg, of the elastic foundation representing the adhesive plus the substructure. As in [1], a glass plate of thickness h_p = 1.27mm, Young's Modulus E_p = 70 GPa and Poisson's ratio ν = 0.24 (yielding D=12.5 N-m) was used in the calculations of k. In Figs. 6 and 7, the stresses and slope errors in the vertex edge zone are plotted for the data in Table 1.

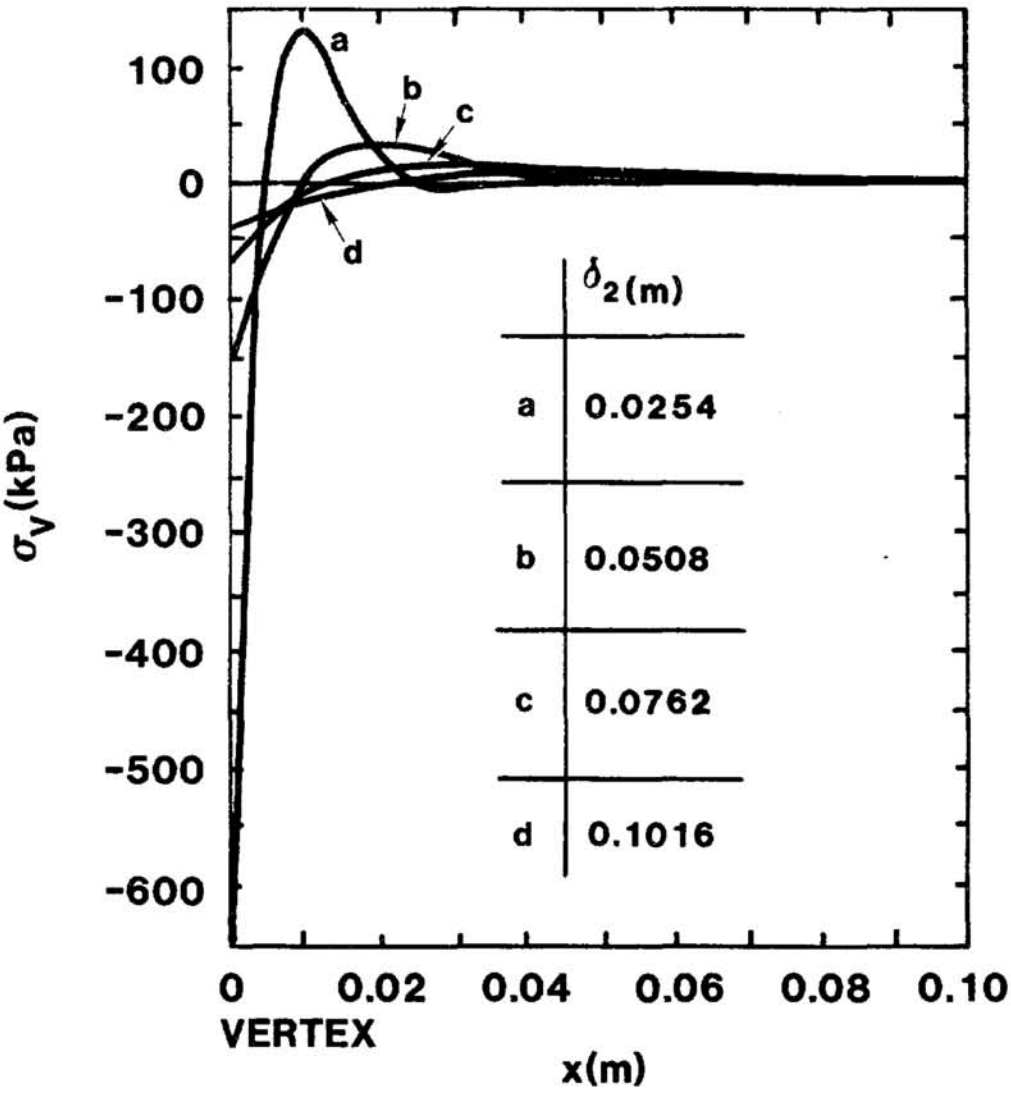

FIGURE 6. Contact stresses in adhesive applied to backside of deformed reflective surface arising from edge effect at vertex.

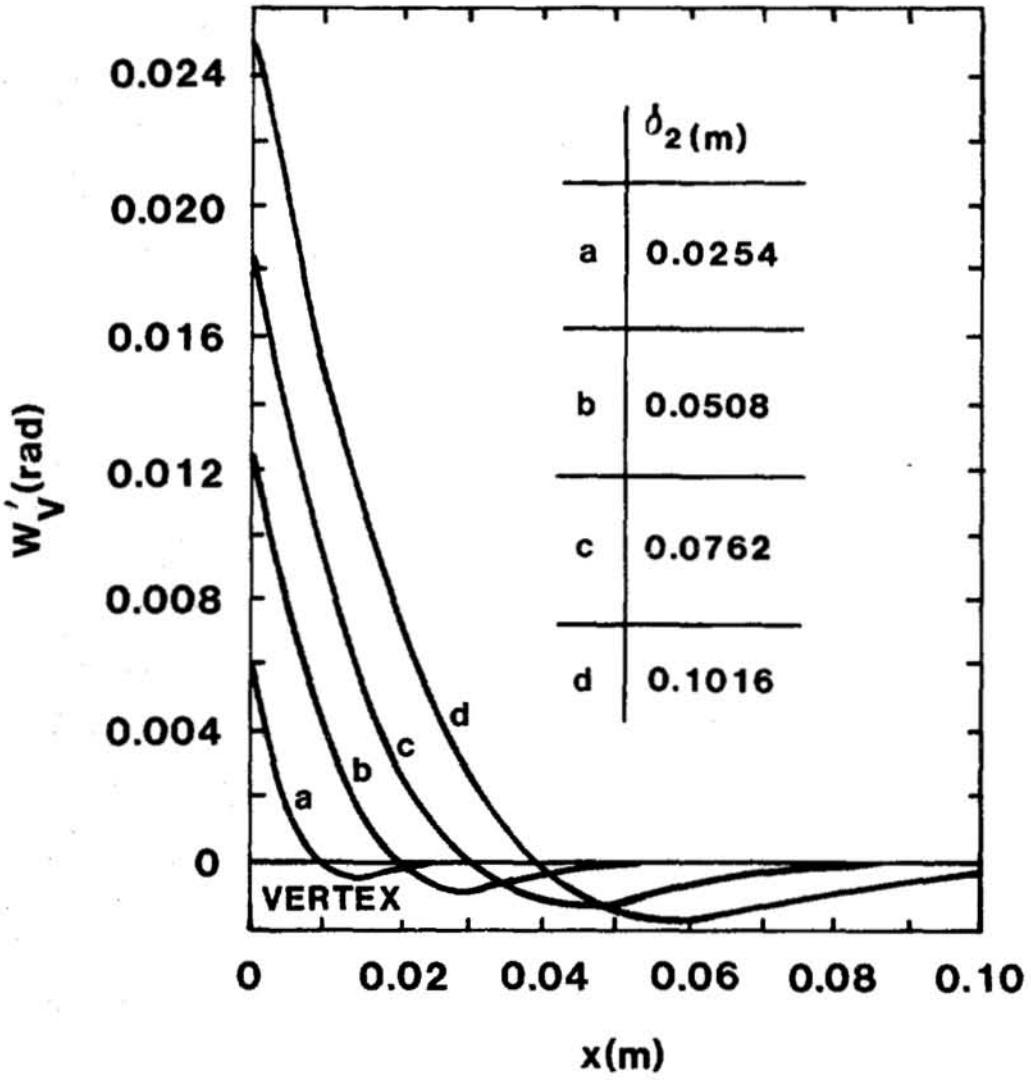

FIGURE 7. Rotation of surface normals (slope error) arising from edge effect at vertex.

TABLE 1

Edge Effect Parameters

δ_2(m)	0.0127	0.0254	0.0508	0.0762	0.1016
$\beta(m^{-1})$	308.4	154.61	77.3	51.5	38.6
k(N-m)	1.900x10	1.188×10^5	7.426×10^2	1.467×10^2	4.639×10^1

To determine the shear stress distribution, $\tau_v(x)$, consider a flat, semi-infinite plate resting on an elastic layer with a force, equal in magnitude and opposite in direction to N_v, applied to the plate at the vertex (Fig. 6). The equation for determining the shear stress in the adhesive is given by [3] as

$$\frac{d^2\tau_v}{dx^2} - 4\gamma^2\tau_v = 0 \ , \tag{14}$$

where

$$\gamma^2 = \frac{G_a}{4E_p h_p h_a} \ . \tag{15}$$

In (15), G_a is the shear modulus of the adhesive and h_a is its thickness. The boundary conditions associated with (14) are

$$\tau_v(x)\Big|_{x=2f} = 0 \ , \tag{16}$$

$$\int_0^{2f} \tau_v(x)dx = N_v \ , \tag{17}$$

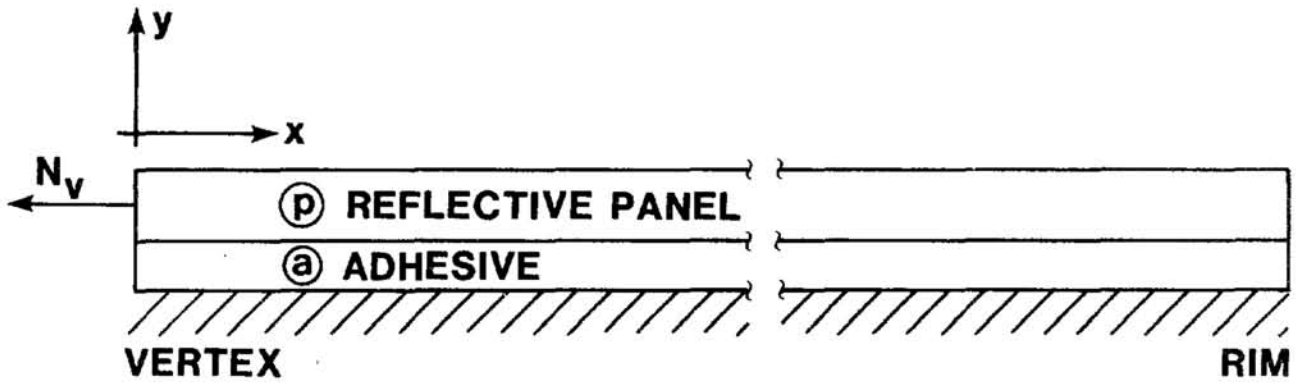

FIGURE 8. Diagram of the flat plate model used to analyze shear deformation arising from edge effect at vertex.

where (17) is the equation for equilibrium in the x direction. The solution to (14), subject to (16) and (17), is given by

$$\tau_v(x) = \frac{2\gamma N_v}{\cosh 4\gamma f - 1} [\sinh(4\gamma f)\cosh(2\gamma x) - \cosh(4\gamma f)\sinh(2\gamma x)]. \quad (18)$$

By noting that for focal lengths of interest $\cosh 4\gamma f >> 1$ and $\tanh 4\gamma f \approx 1$, (18) can be simplified to read

$$\tau_v(x) \simeq 2\gamma N_v [\cosh 2\gamma x - \sinh 2\gamma x] . \quad (19)$$

In Table 2 are some typical values of the plate and adhesive properties, with the corresponding shear stress distributions shown in Fig. 9.

TABLE 2

Typical Values of Panel and Adhesive Properties

	CASE I	CASE II	CASE III
E_p(Pa)	6.895×10^{10}	6.895×10^{10}	6.895×10^{10}
ν	.240	.240	.240
h_p(mm)	0.76	1.27	1.27
h_a(mm)	0.5	0.5	0.38
G_a(Pa)	2.068×10^{8}	2.068×10^{8}	2.068×10^{9}

DISCUSSION OF RESULTS

The curves showing the normal stress distribution and slope errors in the edge effect region near the vertex, Figs. 6 and 7, can be compared with the corresponding curves for the edge effect at the rim, Figs. 3 and 4, to show that the effect is more pronounced at the vertex. Stress levels at the vertex are approximately twice those at the rim and, similarly, the maximum slope error is approximately two times larger at the vertex. However, since the distance from the vertex to the focal line, f, is half the distance from the rim to the focal line, 2f, the distance by which the reflected rays from the two locations miss the focal line, w'f, is approximately the same. The significance of the higher slope errors at the vertex is further mitigated by virtue of receiver tube shadowing. Because of the large stresses in the edge effect zone near the vertex, however, any delamination problems would be expected to occur there first. Maximum tensile stresses occur slightly away from the vertex edge (between δ_1 and δ_2), Fig. 6, and it is conceivable that a delamination initiated there would arrest itself, creating significantly greater slope errors in the process. The delamination would grow away from the vertex because of the compressive stresses which will always reside at the edge, and an arrest would take place when the delamination grew to a size representative of a large enough edge effect zone to reduce stresses sufficiently.

Laser ray tracings showing slope errors are plotted in Figs. 10 and 11 to emphasize the agreement between the above results and experiment. Not only are the edge effects at the vertex and rim clearly defined but the difference in the magnitudes of the slope errors in the two locations are also evident. In Fig. 12, data from Fig. 11 has been superimposed on the anlytical results to show the correlation between theory and experiment. It is emphasized here that this correlation is only in regard to the edge effect. Away from the free ends of

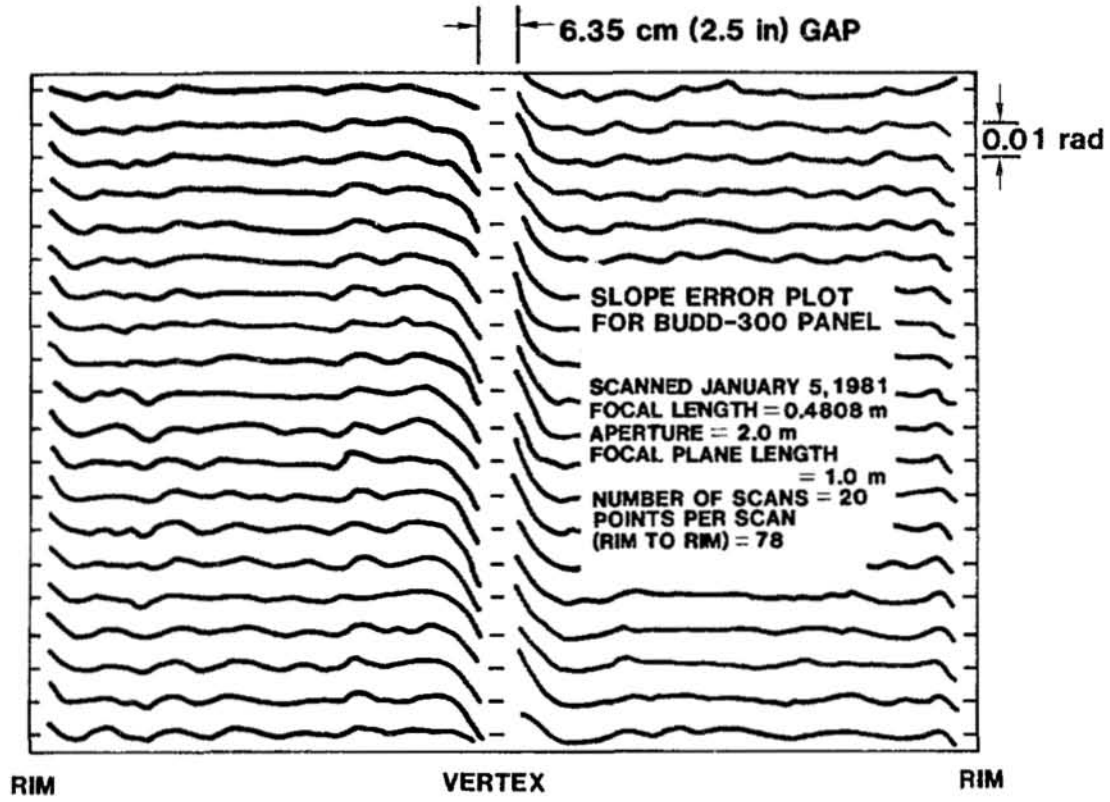

FIGURE 10. Typical results from laser ray tracing showing slope errors at rim and vertex.

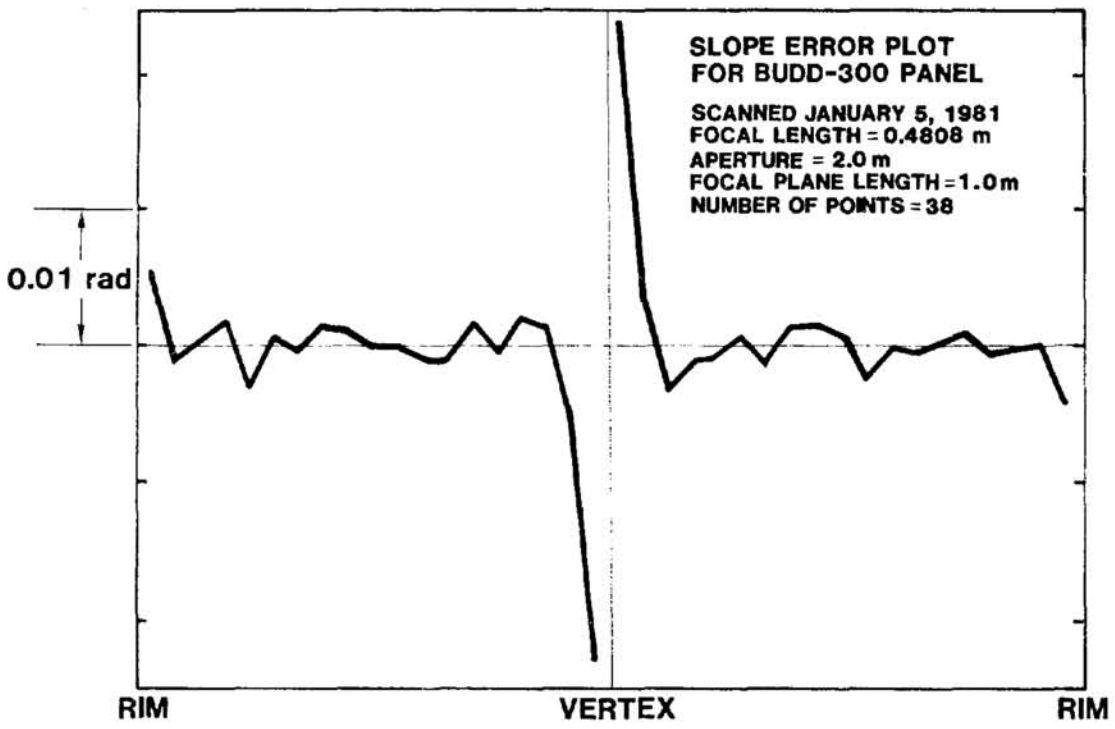

FIGURE 11. Single scan taken from laser ray tracing showing slope errors at rim and vertex.

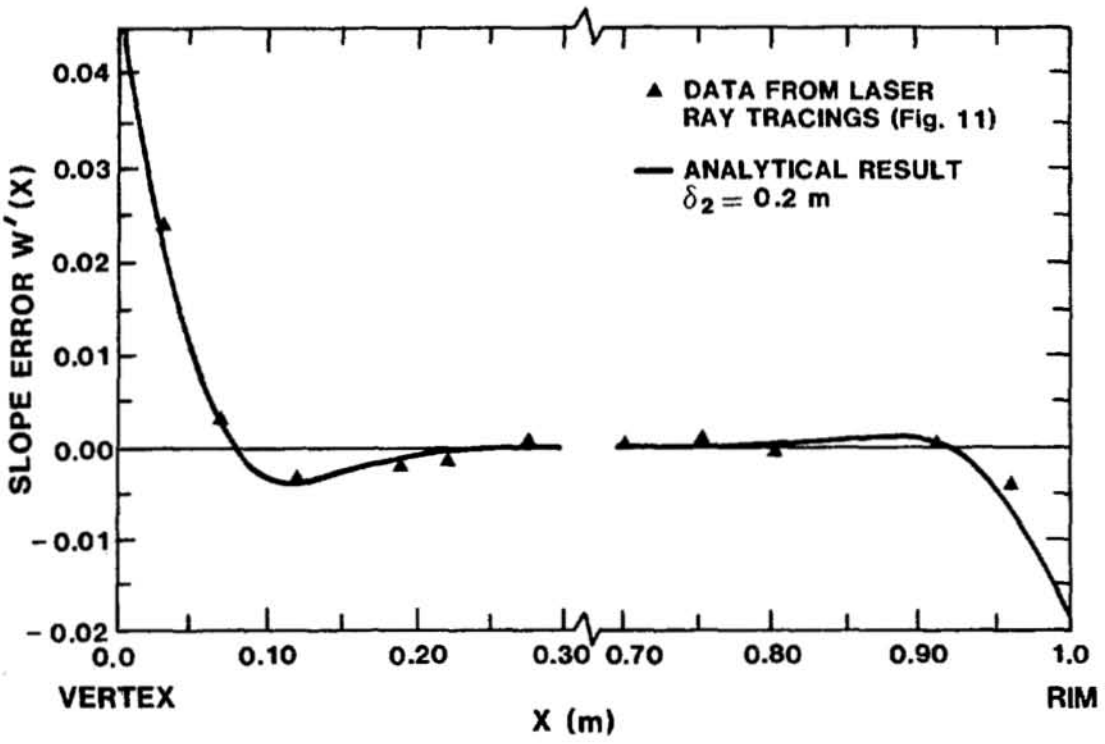

FIGURE 12. Correlation between analytical results [eqs (7) and (13)] and laser ray tracing data (Fig. 11).

the collector, anomalies associated with the substructure introduce additional effects, though relatively small, which are shown in the experimental results (Figs. 11 and 12) but which are not introduced into the analytical model.

Finally, a glance at Fig. 9 shows that the consequences of shear stress due to edge effects are negligible, even for the weakest of back surface coatings or adhesives.

REFERENCES

1. Reuter, R. C., Jr., and Wilson, R. K., "Contact Stresses on a Thin Plate After Large Displacements to a Full Parabolic Surface," Sandia National Laboratories, Report No. SAND81-2083 (1981).

2. Boresi, A. P., Sidebottom, O. M., Seely, F. B., and Smith, J. O., Advanced Mechanics of Materials, 3rd Edition, John Wiley & Sons, NY, NY (1978).

3. Goland, M. and Reissner, E., "The Stresses in Cemented Joints," J. Appl. Mech., Trans. ASME 66, A-17 (1944).

4. Hansche, B. D., "Laser Ray Trace Testor for Parabolic Solar Collectors, "Instrum. Soc. of Am. Proceedings, Vol. 19, No. 2, p. 43 (1980).

Distribution to:
AAI Corporation
P. O. Box 6787
Baltimore, MD 21204

Acurex Aerotherm
485 Clyde Avenue
Mountain View, CA 94042
Attn: J. Vindum

Alpha Solarco
1014 Vine Street
Suite 2230
Cincinnati, OH 45202

Argonne National Laboratory (3)
9700 South Class Avenue
Argonne, IL 60439
Attn: K. Reed
W. W. Schertz
R. Winston

BDM Corporation
1801 Randolf Street
Albuquerque, NM 87106
Attn: T. Reynolds

Black and Veatch (2)
P. O. Box 8405
Kansas City, MO 64114
Attn: Dr. J. C. Grosskreutz
D. C. Gray

Budd Company (2)
Fort Washington, PA 19034
Attn: W. W. Dickhart
W. Eggert

Custom Engineering, Inc.
2805 South Tejon St.
Englewood, CO 80110
Attn: C. A. de Moraes

Del Manufacturing Co.
905 Monterey Pass Road
Monterey Park, CA 91754
Attn: M. M. Delgado

Donnelly Mirrors, Inc.
49 West Third Street
Holland, MI 49423
Attn: J. A. Knister

E-Systems, Inc.
Energy Tech. Center
P. O. Box 226118
Dallas, TX 75266
Attn: R. R. Walters

Edison Electric Institute
90 Park Avenue
New York, NY 10016
Attn: L. O. Elsaesser

Electric Power Research
Institute (2)
3412 Hillview Avenue
Palo Alto, CA 94303
Attn: Dr. J. Cummings
J. E. Bigger

Florida Solar Energy Center (2)
300 State Road, Suite 401
Cape Canaveral, FL 32920
Attn: C. Beech
D. Block

General Atomic
P. O. Box 81608
San Diego, CA 92138
Attn: A. Schwartz

General Electric Co. (2)
P. O. Box 8661
Philadelphia, PA 19101
Attn: W. Pijawka
C. Billingsley

General Motors Corporation
Technical Center
Warren, MI 48090
Attn: J. F. Britt

Georgia Institute of Technology
Atlanta, GA 30332
Attn: J. D. Walton

Haveg Industries, Inc.
1287 E. Imperial Highway
Santa Fe, Springs, CA 90670
Attn: J. Flynt

Hexcel
11711 Dublin Blvd.
Dublin, CA 94566
Attn: R. Johnston

Honeywell, Inc.
Energy Resources Center
2600 Ridgeway Parkway
Minneapolis, MN 55413
Attn: J. R. Williams

Jacobs Engineering Co.
251 South Lake Avenue
Pasadena, CA 91101
Attn: R. Morton

Jet Propulsion Laboratory (3)
4800 Oak Grove Drive
Pasadena, CA 91103
Attn: J. Becker
J. Lucas

Los Alamos Scientific Lab. (3)
Los Alamos, NM 87545
Attn: J. D. Balcomb
C. D. Bankston
D. P. Grimmer

McDonnell-Douglas Astronautics Company (3)
5301 Bolsa Avenue
Huntington Beach, CA 92647
Attn: J. B. Blackmon
J. Rogan
D. Steinmeyer

New Mexico State University
Solar Energy Department
Las Cruces, NM 88001

Office of Technology Assessment
U. S. Congress
Washington, DC 20510
Attn: R. Rowberg

Owens-Illnois
1020 N. Westwood
Toledo, OH 43614
Attn: Y. K. Pei

PPG Industries, Inc.
One Gateway Center
Pittsburg, PA 15222
Attn: C. R. Frownfelter

PRC Energy Analysis Company
7600 Old Springhouse Road
McLean, VA 22101

Parsons of California
3437 S. Airport Way
Stockton, CA 95206
Attn: D. R. Biddle

Schott America
11 East 26th St.
New York, NY 10010
Attn: J. Schrauth

Solar Energy Information Center
1536 Cole Blvd.
Golden, CO 80401
Attn: R. Ortiz

Solar Energy Research Institute (13)
1536 Cole Blvd.
Golden, CO 80401
Attn: B. L. Butler
L. G. Dunham (4)
B. P. Gupta
F. Kreith
J. Thornton
K. Touryan
N. Woodley
D. W. Kearney
C. Bishop
B. Feasby
M. Murphy

Solar Kinetics, Inc.
P. O. Box 47045
8120 Chancellor Row
Dallas, TX 75247
Attn: G. Hutchison

Southwest Research Institute
P. O. Box 28510
San Antonio, TX 78284
Attn: D. M. Deffenbaugh

W. B. Stine
317 Monterey Rd., Apt. 22
South Pasadena, CA 91303

Suntec Systems, Inc.
2101 Wooddale Drive
St. Paul, MN 55110
Attn: L. W. Rees

U. S. Department of Energy (3)
Albuqueque Operations Office
P. O. Box 5400
Albuquerque, NM 87185
Attn: G. N. Pappas
C. B. Quinn
J. Weisiger

U. S. Department of Energy
Division of Energy Storage
Systems
Washington, DC 20545
Attn: J. Gahimer

U. S. Department of Energy (8)
Division of Solar Thermal
Energy Systems
Washington, DC 20545
Attn: W. W. Auer
G. W. Braun
J. E. Greyerbiehl
W. Hocheiser
J. E. Rannels
F. Wilkins
D. Stogowski

U. S. Department of Energy (2)
San Francisco Operations Office
1333 Broadway, Wells Fargo Bldg.
Oakland, CA 94612
Attn: R. W. Hughey

University of New Mexico (2)
Department of Mechanical Eng.
Albuquerque, NM 87113
Attn: M. W. Wilden
W. A. Cross

Viking
3467 Ocean View Blvd.
Glendale, CA 91208
Attn: G. Guranson

2540 K. L. Gillespie
2541 C. M. Gabriel
2542 R. S. Pinkham
3141 L. J. Erickson (5)
3151 W. L. Garner (3)
3161 J. E. Mitchell
4000 A. Narath
4700 J. H. Scott
4710 G. E. Brandvold
4715 R. H. Braasch
4716 J. F. Banas (100)
4717 J. A. Leonard
4720 D. G. Schueler
4750 V. L. Dugan
5000 J. K. Galt
5500 O. E. Jones
5510 D. B. Hayes
5513 D. W. Larson
5520 T. B. Lane
5522 T. G. Priddy
5522 R. K. Wilson (15)
5523 R. C. Reuter, Jr. (15)
5523 D. B. Clauss
5523 J. R. Koteras
5523 B. A. Lewis
5530 W. Herrmann
5814 F. P. Gerstle, Jr.
6011 Patents
8120 W. E. Alzheimer
8123 D. J. Bammann
8214 M. A. Pound
8450 C. Selvage
8450 R. C. Wayne
3154-3 For DOE/TIC (25)
(Unlimited Release)